

Supporting Information for “Radial Structure of the Earth: (I) Model Concepts and Data”

P. Moulik¹ and G. Ekström²

¹Department of Geosciences, Princeton University, Princeton, NJ 08544, USA.

²Lamont-Doherty Earth Observatory of Columbia University, Palisades, NY 10964, USA

Contents

1. Figures S1 to S21

Introduction

Sensitivity kernels of various normal modes to radial (degree-0) structure are provided in Figures S1 and S2. The reference datasets used during construction of the new radial reference Earth model (REM1D, Paper II) are calculated from various published and unpublished measurements contributed by the global geoscience community (Figures S3–S19). The mode eigenfrequencies are plotted relative to the values predicted by PREM (Dziewoński & Anderson, 1981). The procedure for calculating uncertainties is described in Section 2.2 of Paper I. Figure S20 shows that the distribution of bounce points in SS-precursor datasets are biased and some of these regions correspond to strong depressions (>15 km) in the 650-km discontinuity beneath the circum-Pacific subduction zones. Figure S21 provides a zoomed-in version of Figure 10 in Paper I and demonstrates that non-linear crustal contributions to the phase velocities of fundamental-mode surface waves are substantial even for the longer periods of vibration (i.e. frequencies lower than 15 mHz). The reference dataset (e.g. Figures S3–S19), REM1D model (Paper II) and codes to evaluate physical parameters at arbitrary locations are available from the project webpage (<http://rem3d.org>) and are permanently archived on Zenodo (<https://doi.org/10.5281/zenodo.8407693>).

References

- Dahlen, F. A., & Tromp, J. (1998). *Theoretical Global Seismology*. Princeton Univ Press.
- Dziewoński, A. M., & Anderson, D. L. (1981). Preliminary reference Earth model. *Physics of the Earth and Planetary Interiors*, 25, 297–356.
- Gu, Y. J., & Dziewoński, A. M. (2002). Global variability of transition zone thickness. *Journal of Geophysical Research: Solid Earth*, 107. doi: 10.1029/2001jb000489
- Gu, Y. J., Dziewoński, A. M., & Ekström, G. (2003). Simultaneous inversion for mantle shear velocity and topography of transition zone discontinuities. *Geophys. J Int.*, 154, 559–583.
- Mochizuki, E. (1986). The free oscillations of an anisotropic and heterogeneous Earth. *Geophysical Journal International*, 86(1), 167–176.
- Moulik, P., & Ekström, G. (2014). An anisotropic shear velocity model of the Earth’s mantle using normal modes, body waves, surface waves and long-period waveforms. *Geophysical Journal International*, 199, 1713–1738. doi: 10.1093/gji/ggu356

Corresponding author: P. Moulik, moulik@caa.columbia.edu

- Moulik, P., & The 3D Reference Earth Model (REM3D) Consortium. (2022). *Three-dimensional Reference Earth Model Project: Data, Techniques, Models & Tools*. American Geophysical Union (AGU) Fall Meeting, Chicago, IL, USA. doi: 10.5281/zenodo.7883683
- Shearer, P. M. (1991). Constraints on upper mantle discontinuities from observations of long-period reflected and converted phases. *Journal of Geophysical Research: Solid Earth*, 96 (B11), 18147–18182. doi: 10.1029/91jb01592
- Waszek, L., & Deuss, A. (2015). Observations of exotic inner core waves. *Geophysical Journal International*, 200(3), 1636–1650. doi:10.1093/gji/ggu497
- Wei, S. S., & Shearer, P. M. (2017). A sporadic low-velocity layer atop the 410 km discontinuity beneath the Pacific Ocean. *Journal of Geophysical Research: Solid Earth*, 122 (7), 5144–5159. doi:10.1002/2017jb014100

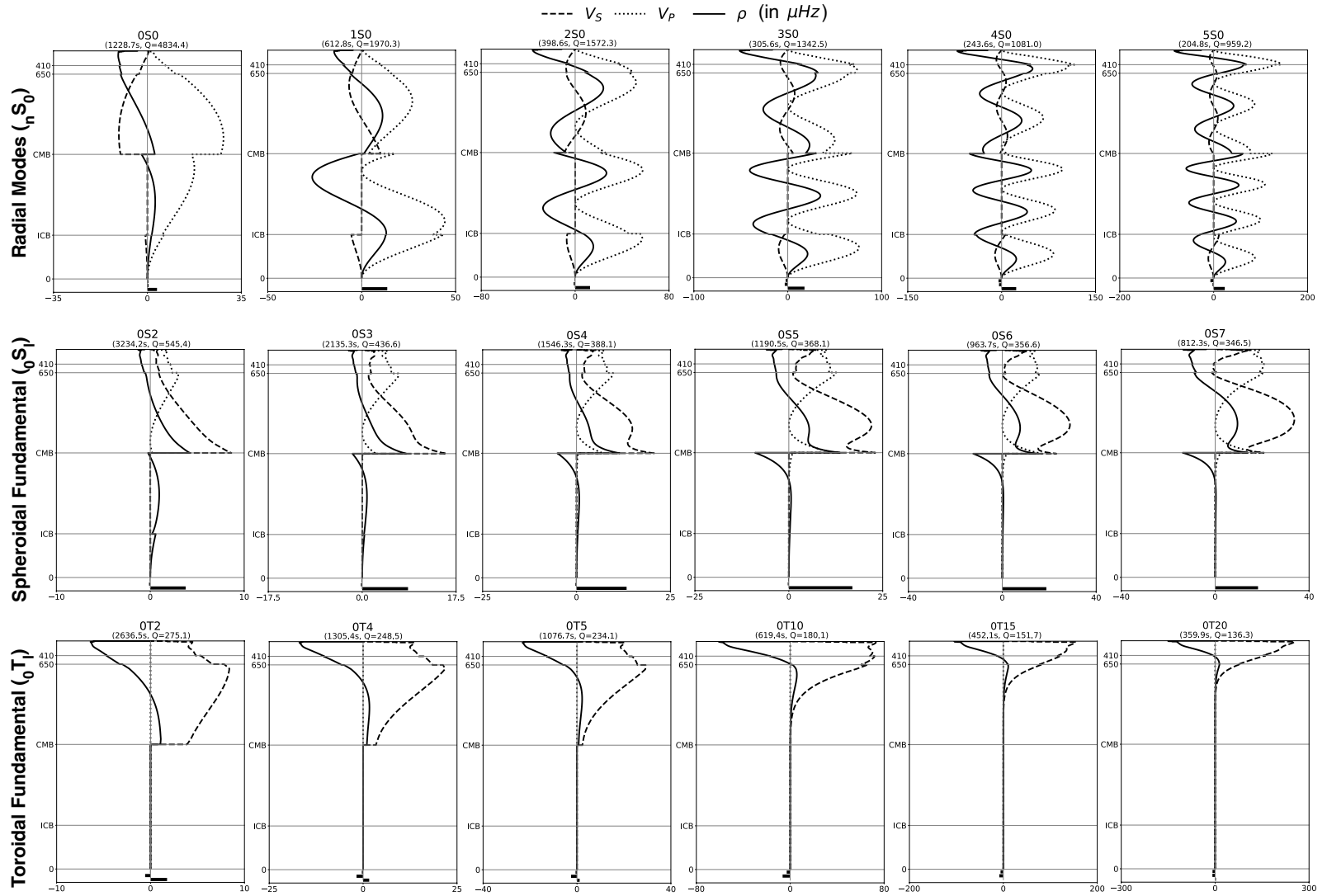


Figure S1. Sensitivity kernels of radial and fundamental normal modes to the degree 0 variations in density and Voigt-averaged shear and compressional velocities (v_P , v_S). Depth of the 410-km and 650-km discontinuities and the CMB are indicated by grey horizontal lines. Horizontal bars beneath the kernels show from top to bottom, the mode's sensitivity to topographic perturbations of the 410 and 650-km discontinuities and the CMB (K_{410}^0 , K_{650}^0 & K_{CMB}^0). Note that the kernels are calculated using REM1D (Paper II), are in units of μHz and correspond to variations in physical parameters ($\delta m_i/m_i$) or topography ($\delta h/a$) of 1%, where $a=6371$ km and that each graph is scaled independently. Note the strong sensitivity of radial modes to v_P and density throughout the Earth, and that of spheroidal fundamental and toroidal modes to v_S and density in the mantle. Normal modes are able to constrain both stratification (i.e. gradient) and magnitude of physical properties due to their oscillatory sensitivity kernels (Mochizuki, 1986; Dahlen & Tromp, 1998); an increase in density, for example, can either have a positive or negative effect on eigenfrequencies of toroidal modes (angular order 2, ${}_nS_2$) depending on the depth of perturbation. Note that we employ anisotropic kernels in our inversions for radial structure (Figure S2).

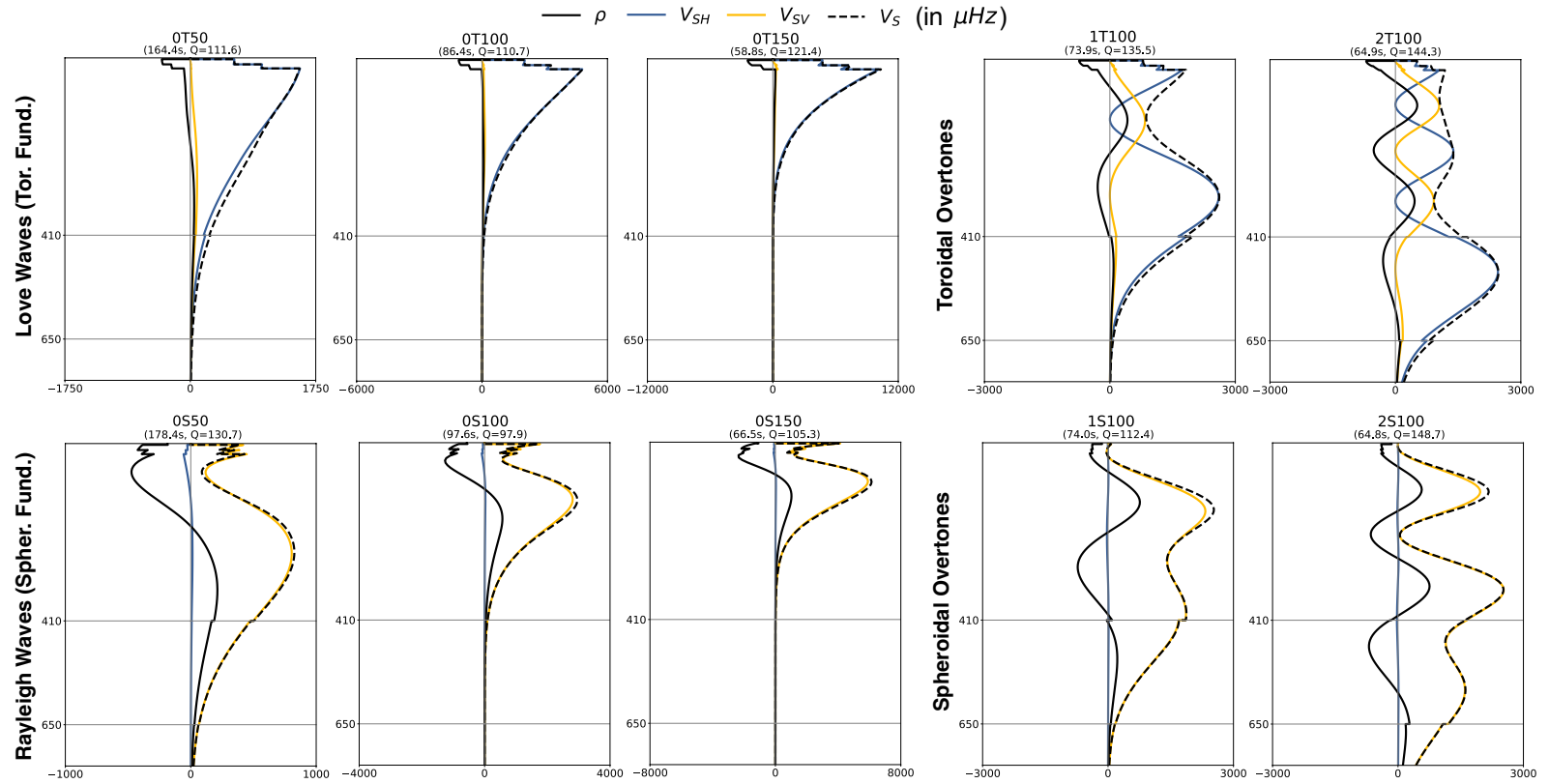


Figure S2. Sensitivity kernels of several normal modes to the degree 0 variations in density (ρ), anisotropic shear velocities (v_{SH} , v_{SV}), and Voigt-averaged isotropic velocity (v_S). Depth of the 410-km and 650-km discontinuities in the mantle transition zone are indicated by grey horizontal lines. Note that the kernels are calculated using REM1D (Paper II), are in units of μHz and correspond to variations in physical parameters ($\delta m_i/m_i$) and that each graph is scaled independently. Note that Love-wave equivalent toroidal fundamental modes are sensitive primarily to v_{SH} structure while Rayleigh-wave equivalent spheroidal fundamental modes are sensitive primarily to v_{SV} structure. The depth of strongest sensitivity for fundamental modes becomes shallower at large angular orders (l) and deeper structure may be probed by including overtones ($n > 0$).

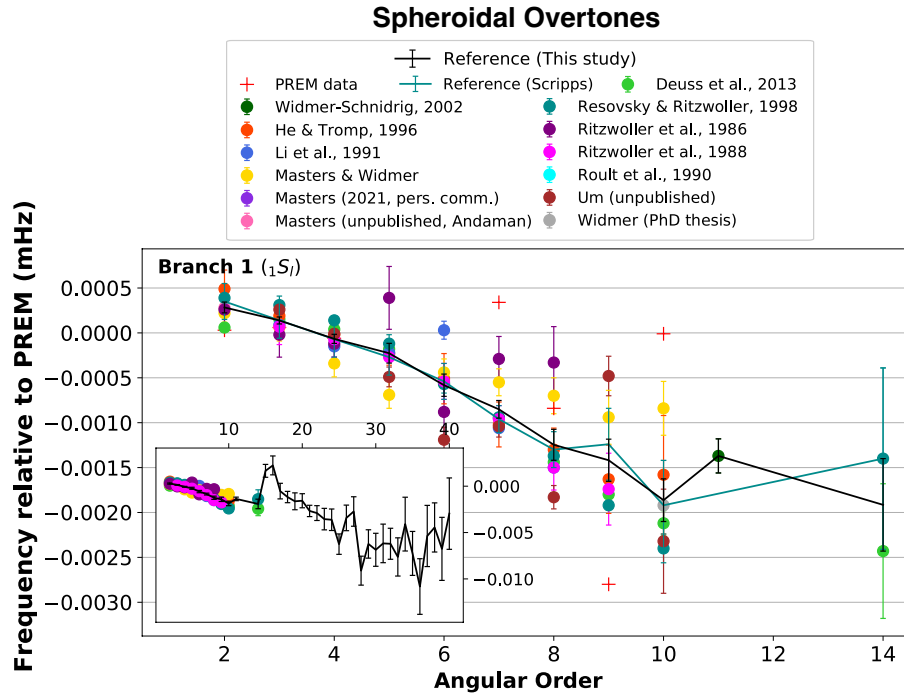


Figure S3. Observed eigenfrequencies of spheroidal modes in the 1st overtone branch. Inset figure shows eigenfrequencies for all angular orders, which include the estimates for overtones from regionalized multiplet stripping (Section 2.1.2). Note the full description in the caption of Figure 1 in Paper I. A small catalog of best estimates from Scripps based on data till the year 2000 is plotted for comparison wherever available (green curves). For clarity, eigenfrequencies are plotted relative to the values predicted by PREM.

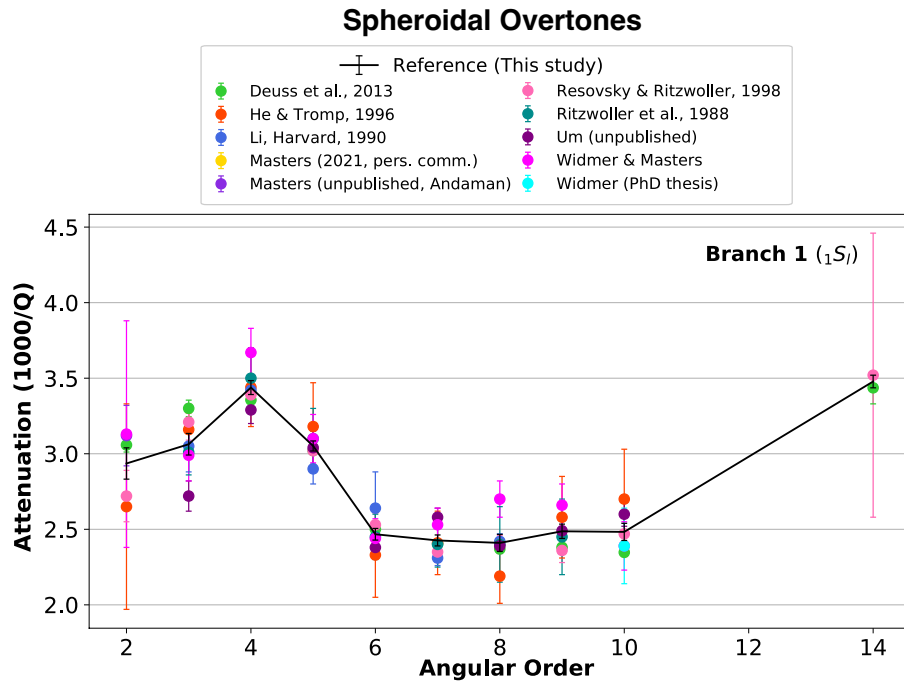


Figure S4. Observed quality factors of spheroidal modes in the 1st overtone branch. Note the full description in the caption of Figure 1 in Paper I.

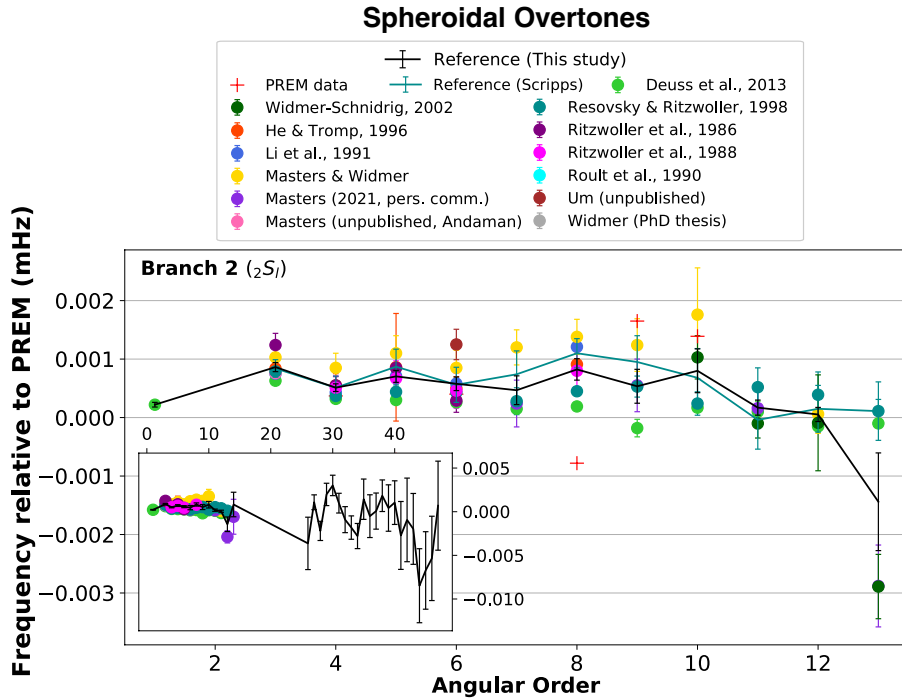


Figure S5. Observed eigenfrequencies of spheroidal modes in the 2nd overtone branch. Inset figure shows eigenfrequencies for all angular orders, which include the estimates for overtones from regionalized multiplet stripping (Section 2.1.2). Note the full description in the caption of Figure 1 in Paper I. A small catalog of best estimates from Scripps based on data till the year 2000 is plotted for comparison wherever available (green curves). For clarity, eigenfrequencies are plotted relative to the values predicted by PREM.

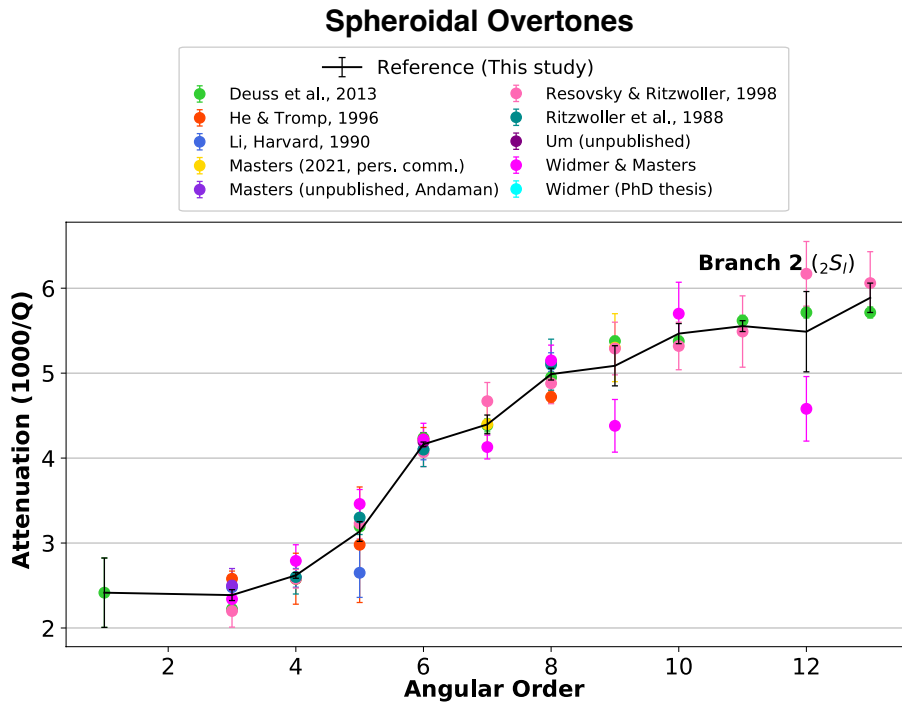


Figure S6. Observed quality factors of spheroidal modes in the 2nd overtone branch. Note the full description in the caption of Figure 1 in Paper I.

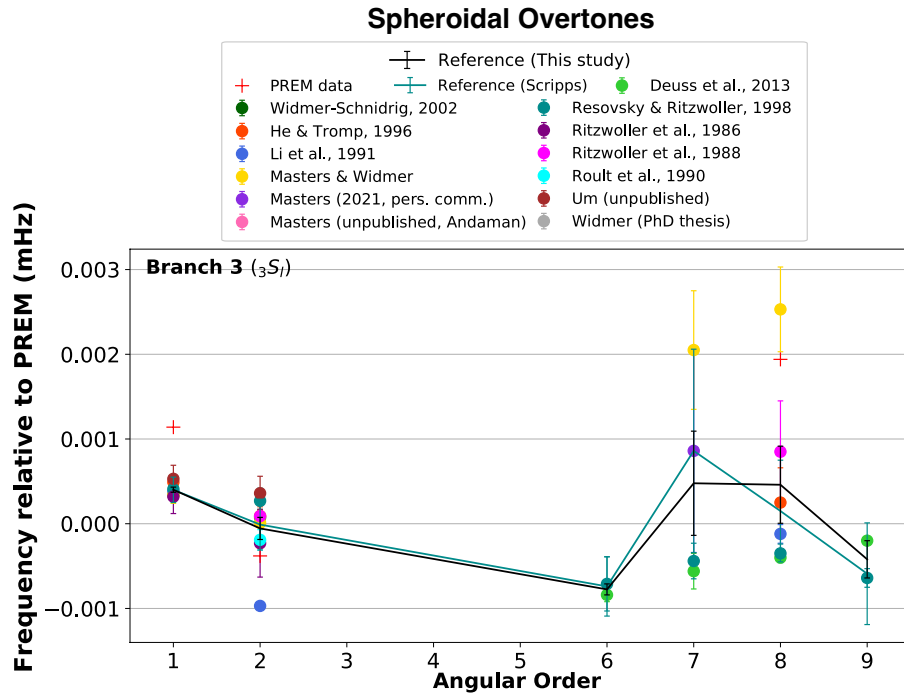


Figure S7. Observed eigenfrequencies of spheroidal modes in the 3rd overtone branch. Note the full description in the caption of Figure 1 in Paper I. A small catalog of best estimates from Scripps based on data till the year 2000 is plotted for comparison wherever available (green curves). For clarity, eigenfrequencies are plotted relative to the values predicted by PREM.

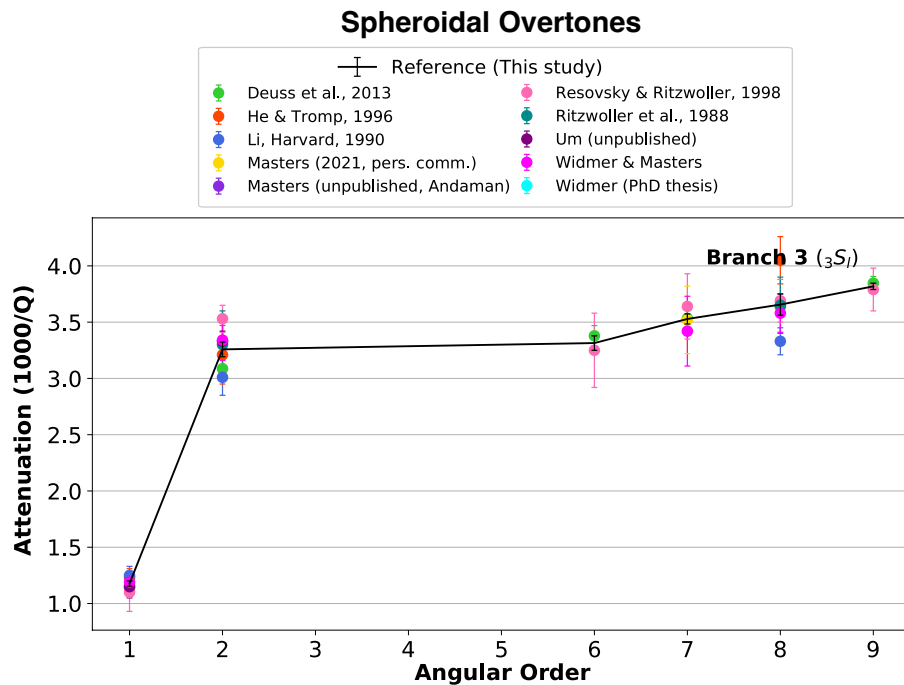


Figure S8. Observed quality factors of spheroidal modes in the 3rd overtone branch. Note the full description in the caption of Figure 1 in Paper I.

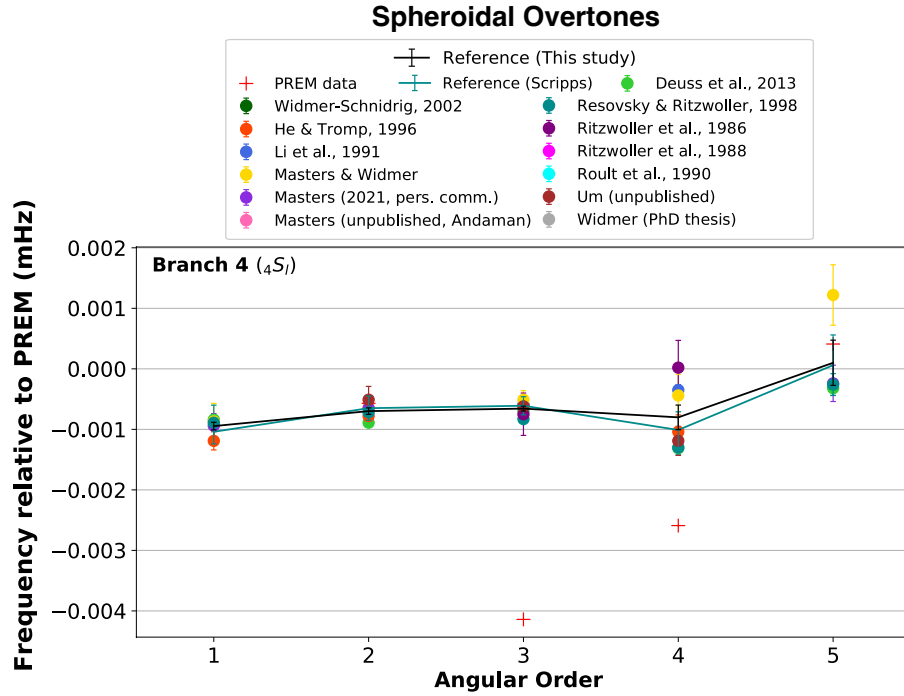


Figure S9. Observed eigenfrequencies of spheroidal modes in the 4th overtone branch. Note the full description in the caption of Figure 1 in Paper I. A small catalog of best estimates from Scripps based on data till the year 2000 is plotted for comparison wherever available (green curves). For clarity, eigenfrequencies are plotted relative to the values predicted by PREM.

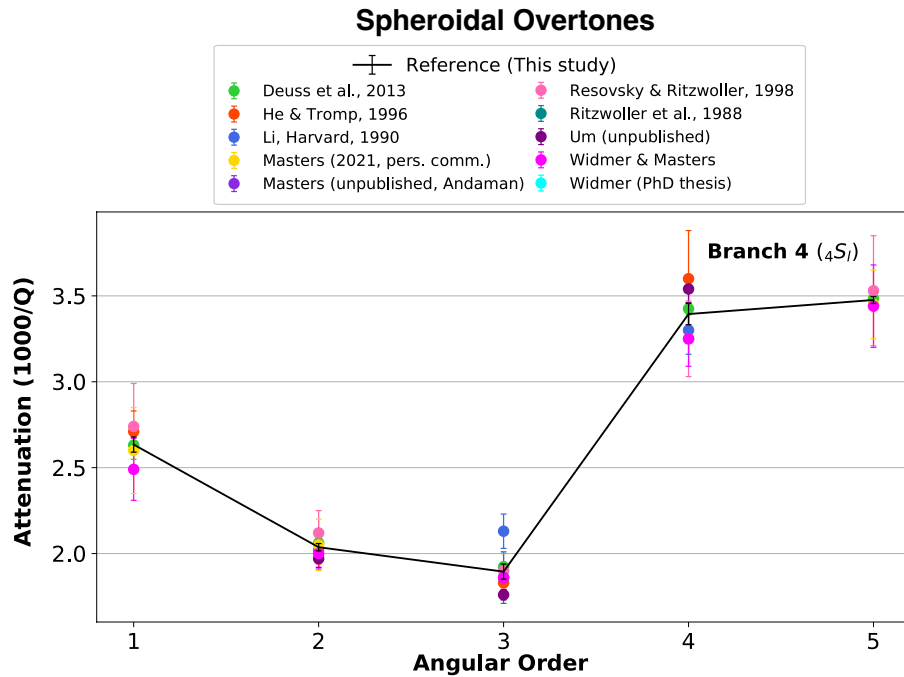


Figure S10. Observed quality factors of spheroidal modes in the 4th overtone branch. Note the full description in the caption of Figure 1 in Paper I.

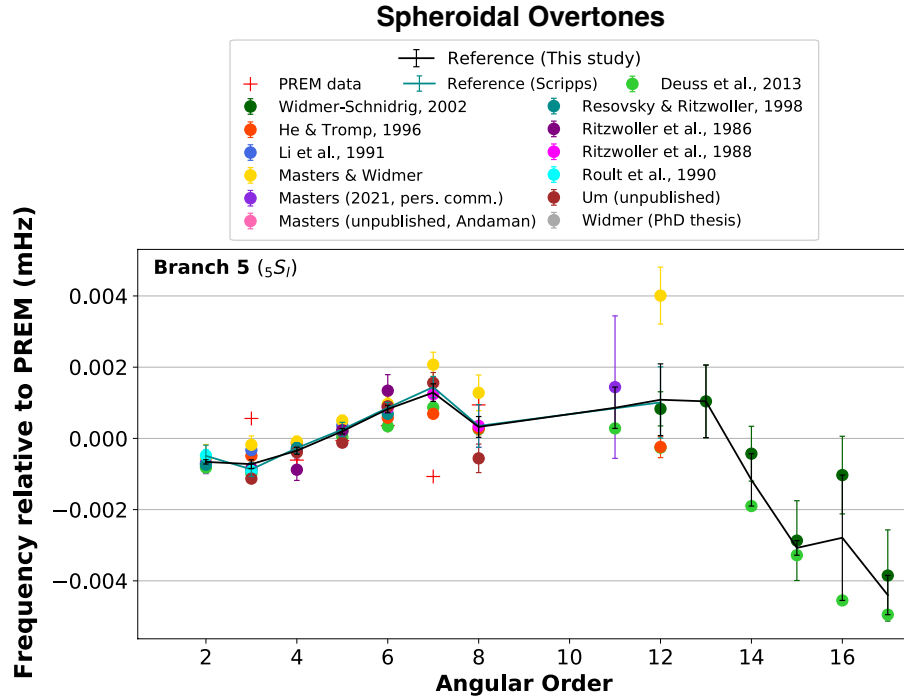


Figure S11. Observed eigenfrequencies of spheroidal modes in the 5th overtone branch. Note the full description in the caption of Figure 1 in Paper I. A small catalog of best estimates from Scripps based on data till the year 2000 is plotted for comparison wherever available (green curves). For clarity, eigenfrequencies are plotted relative to the values predicted by PREM.

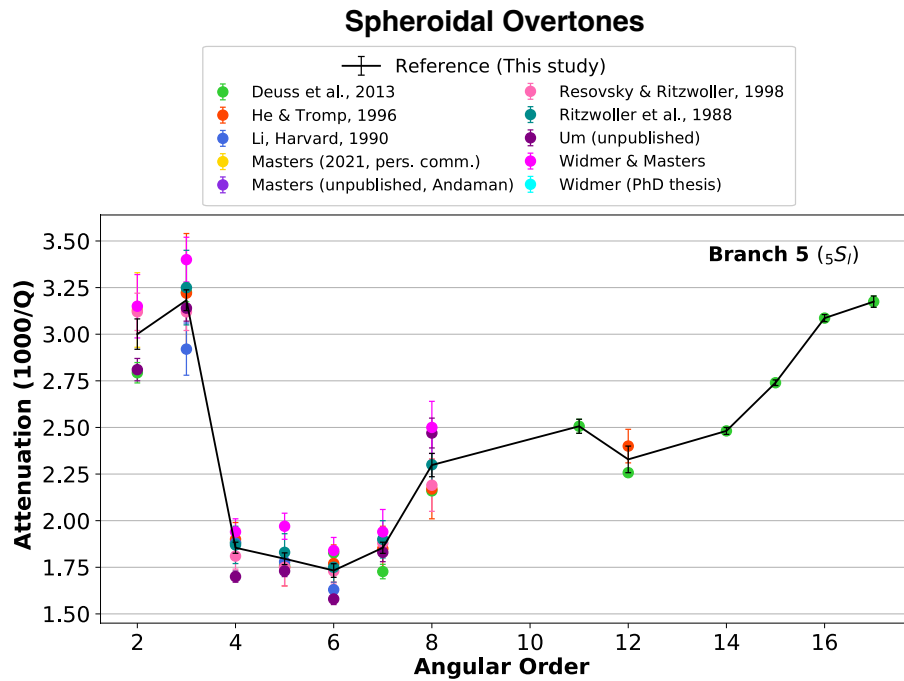


Figure S12. Observed quality factors of spheroidal modes in the 5th overtone branch. Note the full description in the caption of Figure 1 in Paper I.

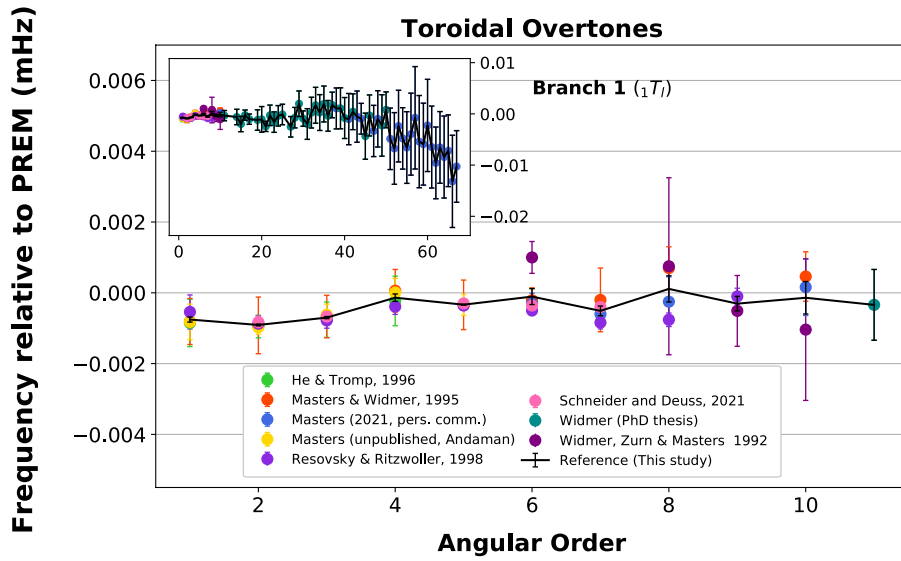


Figure S13. Observed eigenfrequencies of toroidal modes in the 1st overtone branch. Inset figure shows eigenfrequencies for all angular orders, which include the estimates for overtones from regionalized multiplet stripping (Section 2.1.2). Note the full description in the caption of Figure 1 in Paper I. For clarity, eigenfrequencies are plotted relative to the values predicted by PREM.

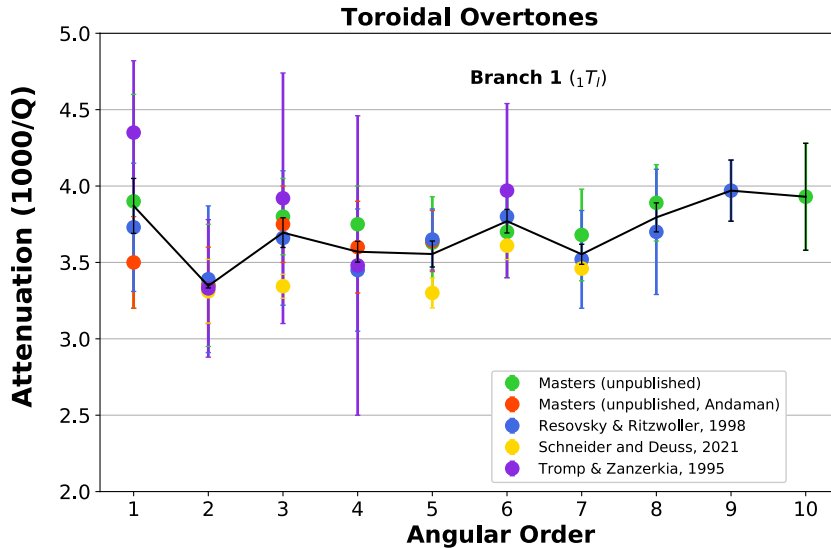


Figure S14. Observed quality factors of toroidal modes in the 1st overtone branch. Quality factors of toroidal modes are only available till the 2th branch. Note the full description in the caption of Figure 1 in Paper I.

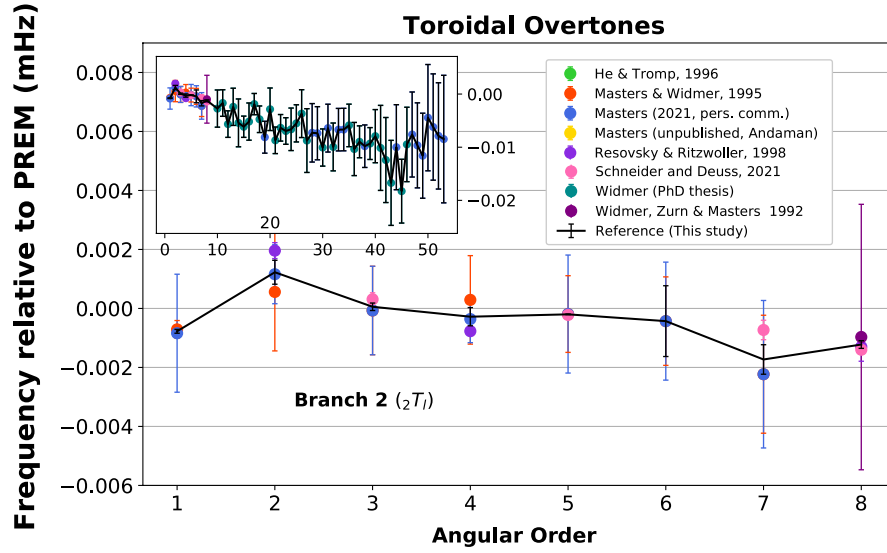


Figure S15. Observed eigenfrequencies of toroidal modes in the 2nd overtone branch. Inset figure shows eigenfrequencies for all angular orders, which include the estimates for overtones from regionalized multiplet stripping (Section 2.1.2). Note the full description in the caption of Figure 1 in Paper I. For clarity, eigenfrequencies are plotted relative to the values predicted by PREM.

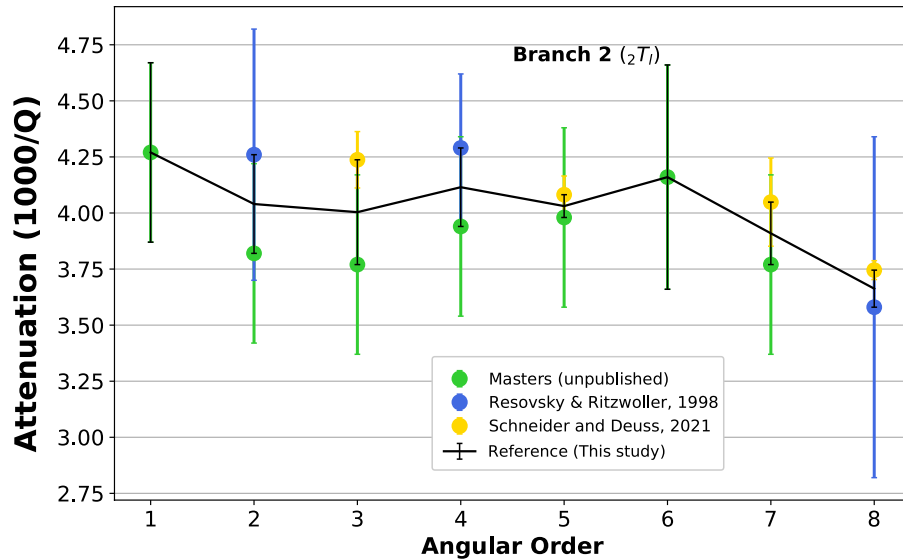


Figure S16. Observed quality factors of toroidal modes in the 2nd overtone branch. Quality factors of toroidal modes are only available till the 2th branch. Note the full description in the caption of Figure 1 in Paper I.

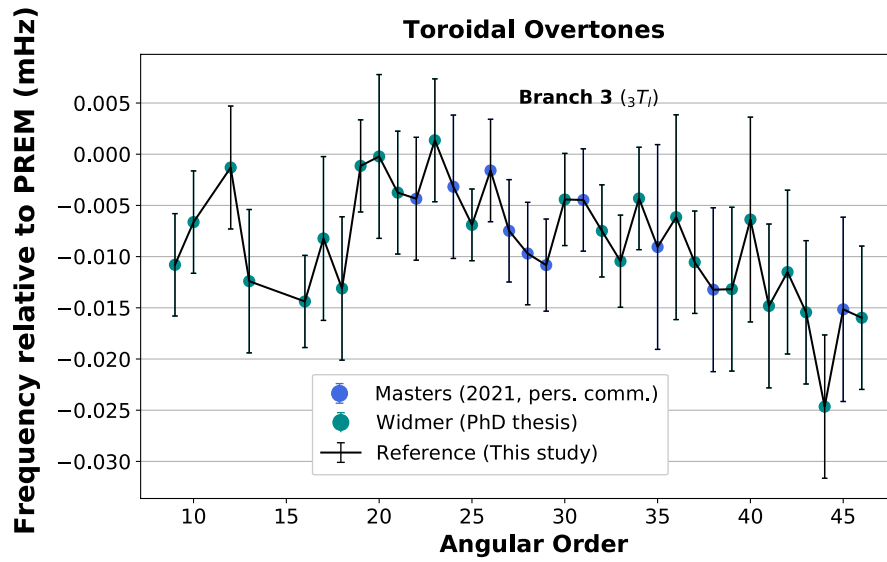


Figure S17. Observed eigenfrequencies of toroidal modes in the 3rd overtone branch. Note the full description in the caption of Figure 1 in Paper I. For clarity, eigenfrequencies are plotted relative to the values predicted by PREM.

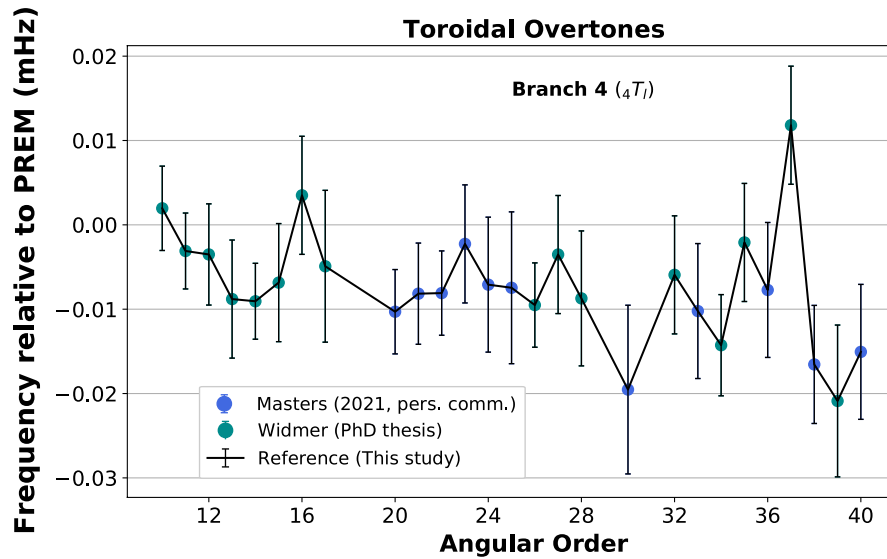


Figure S18. Observed eigenfrequencies of toroidal modes in the 4th overtone branch. Note the full description in the caption of Figure 1 in Paper I. For clarity, eigenfrequencies are plotted relative to the values predicted by PREM.

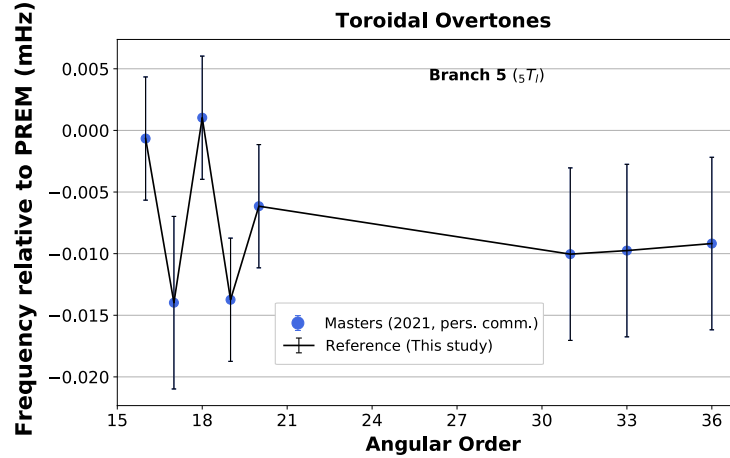


Figure S19. Observed eigenfrequencies of toroidal modes in the 5th overtone branch. Note the full description in the caption of Figure 1 in Paper I. A small catalog of best estimates from Scripps based on data till the year 2000 is plotted for comparison wherever available (green curves). For clarity, eigenfrequencies are plotted relative to the values predicted by PREM.

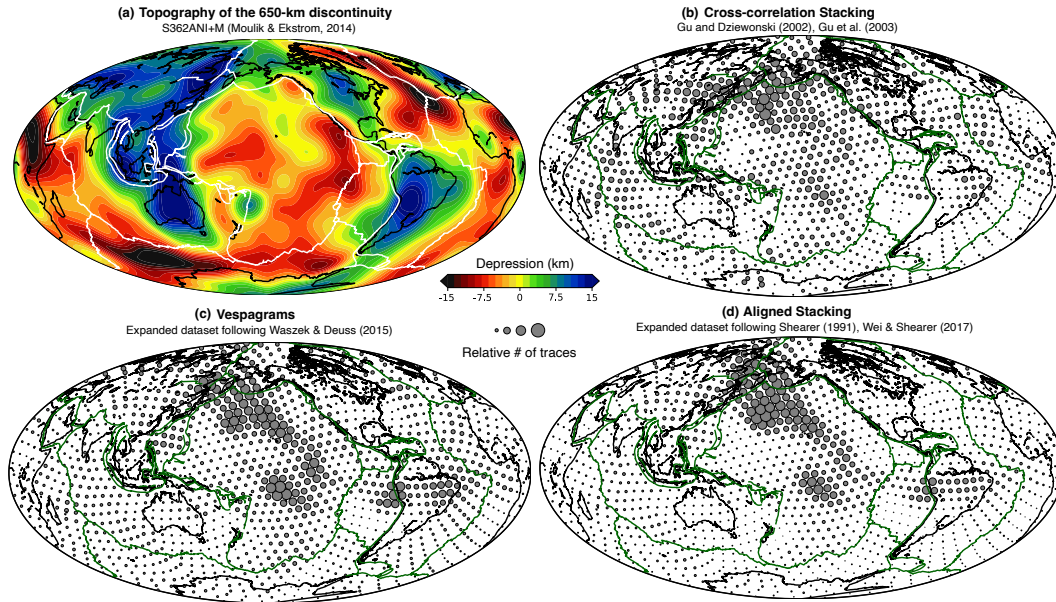


Figure S20. Distribution of bounce points for SS-precursor datasets. (a) Topography of the 650-km discontinuity from the 3D model S362ANI+M (Moulik & Ekström, 2014) constructed using full spectrum tomography (FST), showing strong depressions (>15 km) beneath the circum-Pacific subduction zones. Number of seismogram traces contributing to the 1442 evenly-distributed caps from three techniques, (b) cross-correlation stacking (Gu & Dziewonski, 2002; Gu et al., 2003), (c) vespagrams (Waszek & Deuss, 2015) and, (d) aligned stacking of waveforms (Shearer, 1991; Wei & Shearer, 2017). The number of traces differ by up to an order of magnitude between the three catalogs and the scatter plot is therefore normalized for each catalog. More bounce points are found within and around the Pacific Ocean basin irrespective of the catalog based on the current source-station distribution. The first catalog (b) resolved previously under-sampled regions such as South America, the southern Pacific, Atlantic and Indian Oceans. The latter two catalogs (c,d) contain unpublished data contributed to the REM3D project (Moulik & The 3D Reference Earth Model (REM3D) Consortium, 2022).

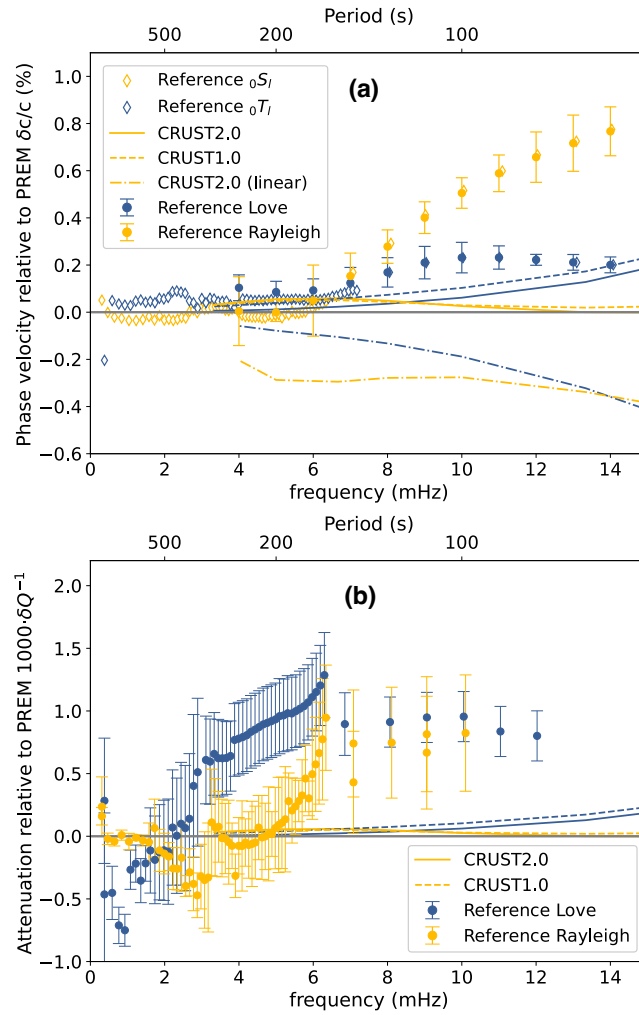


Figure S21. Global averages of perturbations in phase-velocity ($\delta c/c$, a) and attenuation ($1000 \cdot \delta Q^{-1}$, b) for Love (in blue) and Rayleigh waves (in yellow) up to 15 mHz. Note the full description in the caption of Figure 10.